# Molecular Orientation-Dependent Interfacial Energetics and Built-in Voltage Tuned by a Template Graphene Monolayer

Lushuai Zhang,[†] Susmit Singha Roy,[†] Robert J. Hamers,[†,‡] Michael S. Arnold,[†] and Trisha L. Andrew*[,†,‡]

[†]Department of Materials Science and Engineering and [‡]Department of Chemistry, University of Wisconsin-Madison, Madison, Wisconsin 53706, United States

S *Supporting Information*

ABSTRACT: Highly transparent and conductive monolayer graphene was used as a template to tune the crystal orientation of pentacene from generic standing-up (001) to lying-down (022) in neat films. Spatially resolved Kelvin probe force microscopy (KPFM) was used to reveal the energy levels of pentacene thin films grown on substrates with and without the template graphene layer, as well as the energy level alignment in various pentacene-containing organic–organic heterojunctions. A correlation between crystal domain orientation and the work function was directly observed using KPFM. Up to 0.36 eV shifts in work function were observed in neat pentacene films over large areas (>0.5 in.^{2}) upon orientation transition, likely due to the transition from Fermi level pinning (standing-up pentacene on ITO) to vacuum level alignment (lying-down pentacene on graphene–ITO). Morphology-induced energy level shifts versus interfacial electronic equilibration effects were disentangled using atomic force microscopy, KPFM, X-ray diffraction, and Raman data for neat pentacene films and pentacene containing heterojunctions on monolayer graphene. The data detailed herein provide a fundamental picture of the major interfacial effects active in optoelectronic devices containing a bare graphene electrode.
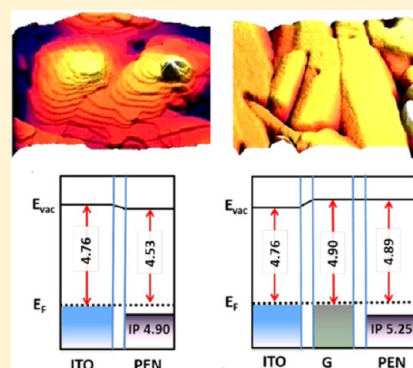
INTRODUCTION

Organic photovoltaic (OPV) devices have the potential to become inexpensive, lightweight, and flexible sources of renewable energy because of the large absorption coefficients and thin-film forming ability of organic materials and because organic semiconductors can be processed at low-temperatures.[1−3] However, the capability to manufacture sustainably >10% efficient OPVs with high throughput is required to ensure competitiveness in contemporary energy markets.[4] Conventional efforts to increase device efficiency are largely synthetic chemistry-driven because the rich chemistry of conjugated small molecules and polymers allows tuning of bulk material properties.[5] Varied device architectures, such as plasmon-enhanced[6,7] and multijunction devices,[8,9] are also promising approaches. Photoactive materials for OPVs are selected based on bulk highest occupied molecular orbital (HOMO) and lowest unoccupied molecular orbital (LUMO) levels, assuming that these values are conserved at hetero-junction interfaces, and minimal attention is paid to quantifying interfacial effects that may alter these bulk values.[5,10−12]

Most OPVs require both a donor and an acceptor material to drive exciton dissociation at the interface between the two components and improve charge collection under operational bias.[13] Thus, organic heterojunction interfaces are pervasive in OPVs and significantly influence charge transfer,[14] exciton dissociation,[15,16] and geminate pair dissociation and recombination events[17,18] that determine device efficiency. Because of the highly anisotropic electronic structures of π-conjugated

molecules, the ionization potentials (IP) and electron affinities (EA) of organic semiconductor thin films are orientation-dependent.[19−22] The electric field across organic–organic heterojunctions is also highly dependent on molecular orientation.[23,24] Thus, various interface interactions become important parameters for tuning electronic coupling across organic–organic heterojunctions and are considered as key factors for determining device performance.[15−18]

Two major characteristics need to be understood for any interface: intermolecular configuration[19] and electronic equilibration. The intermolecular configuration of organic semi-conductors largely affects charge-transfer mobilities[14] and nearest-neighbor transfer integrals (or electronic coupling) both in the bulk and at heterointerfaces.[17,18] Molecular orientation can shift bulk HOMO and LUMO energy levels by up to 1.0 eV,[23,25] which can be partially explained by the following equations:

$$E_{CB} = \mu_e^{\,o} + q\phi \tag{1}$$

$$E_{vB} = \mu_e^{\,o} + q\phi - E_G \tag{2}$$

Equation 1 determines the conduction band edge, and eq 2 determines the valence band edge.[12,21] In these equations, $\mu_e^{\,o}$ is the standard chemical potential and φ is the electrostatic

potential. van der Waals dispersion forces, such as d−π and π−π interactions, usually determine molecular orientations in vapor-deposited thin films.[26−30] These interactions give rise to discrete electrostatic potentials in the condensed phase that modify the intrinsic chemical potential of organic semiconductors. Limited strategies exist that allow precise control over intermolecular configuration in the bulk, and even fewer tactics are known to control molecular orientation at a heterointerface.

Electronic equilibration at a heterointerface can be achieved via charge transfer (resulting in a dipole at the adjacent region of the interface or band-bending over larger distances). Depending on differences in carrier density, density of states, and the energy level mismatch between two materials at an interface, one particular mechanism of electronic equilibration will be favored over another. Electronic equilibration across a heterointerface ultimately determines a number of important device parameters, such as the built-in voltage of a diode; charge injection barriers at an electrode interface;[31−33] and charge-transfer (CT) state formation, relaxation, and/or dissociation in OPVs.[34,35]

Interfacial effects in selected heterojunctions are well-characterized. For example, at interfaces between an organic semiconductor and a metal, strong electronic coupling leads to a change in the work function (ϕ) of the metal via a "pushback effect", which is empirically described by the Helmholtz equation:

$$\Delta \varphi = \frac{eN\mu}{\varepsilon\varepsilon_0} \quad (3)$$

where e is the elementary charge, N the area density of dipoles, μ the dipole moment, ε the relative permittivity, and ε_o the vacuum permittivity. However, the initial model of vacuum level alignment based on the Mott−Schottky limit does not universally describe organic−metal and organic−conductive oxide interfaces.[27,28,36,37] Instead, the integer charge transfer (ICT) and the induced density of interfacial states (IDIS) models are widely preferred. The ICT model applies to systems that do not have hybridized electronic states or partial charge transfer (only integer charge transfer), such as interfaces involving van der Waals interactions. The IDIS model explains energetics of interfaces in which chemical reactions are moderate but non-negligible, such as clean metal−organic semiconductor interfaces.[38] Additionally, the gap states model, which focuses on the contributions of intragap states to Fermi level pinning, successfully explains vacuum level shifts and band-bending phenomena in some metal−organic and organic−organic heterojunctions.[39]

A universal model that applies to all organic heterojunction interfaces is complicated to develop because of polarization and charge-transfer interactions,[10,22,40,41] substrate screening,[42] disordered interface dipoles, and midgap states. Thus, empirical studies of interfaces provide invaluable insight. Ultraviolet photoemission spectroscopy (UPS) and X-ray photoemission spectroscopy (XPS) are popular techniques for studying interfacial electronic characteristics. However, these methods have limits such as (1) organic semiconductors have low intrinsic carrier densities in the dark, which may cause detrimental and misleading sample charging during UPS measurements; (2) UPS requires conductive substrates such as metals, but metal substrates may have strong interactions with the first layer organic semiconductors (OSCs) and readily introduce doping by charge transfer;[43] and (3) X-ray-based methods measure only an average value of the whole sample without distinguishing defects in organic thin films. In contrast, Kelvin probe force microscopy (KPFM) is appropriate for materials with poor electrical properties. KPFM has no specific substrate requirement. KPFM is also a spatially resolved technique, with spatial resolution no larger than 25 nm. Indeed, KPFM has been previously used to probe various morphological and electronic characteristics of organic semiconductors and their heterointerfaces.[44−47]

In this report, the unique interaction between graphene and small molecules[48,49] is used to control both the thin-film morphology and electronic characteristics of pentacene films. KPFM is used to probe the vacuum levels of organic semiconductor layers both on glass and graphene-covered glass. The latter provides a model system to understand electronic energy levels in next-generation devices containing a graphene electrode. Morphology-induced energy level shifts versus interfacial electronic equilibration effects are disentangled using atomic force microscopy (AFM), KPFM, X-ray diffraction (XRD), and Raman data.

■ EXPERIMENTAL METHODS

Pentacene films were prepared by thermal evaporation of source material (TCI sublimed grade) onto monolayer graphene, O_2 plasma-treated glass or ITO with chamber pressures below 1×10^{-6} Torr and a deposition rate of 0.3 Å/s. The film crystallinity and orientation were characterized using a Bruker D8 discover X-ray diffractometer in the $\theta−2\theta$ configuration with Cu Kα (wavelength, 1.542 Å) source and 0.5 mm slit width.

CVD-Graphene Growth. Monolayers of graphene were grown on Cu foils (Alfa Aesar; product 13382, lot B03Y027) as the growth catalyst. The foils were precleaned with acetic acid (Fisher) for 15 min to remove contaminants and native oxides then rinsed in DI water (×3) before being dried with an air-gun. The cleaned Cu foils were then annealed for 30 min at 1030 °C in 95% argon and 5% hydrogen (340 sccm flow rate) to remove trace surface contaminants and also to reduce the surface roughness of the foil before initiating the growth process. The growth was conducted at 1030 °C with 95% argon and 5% methane (0.300 sccm) and 95% argon and 5% hydrogen (340 sccm) for 3 h. The samples of manufactured graphene on Cu foils were stored in a N_2 glovebox to minimize the oxidation of the graphene and the copper surfaces.

Graphene Transfer. Graphene monolayers grown via chemical vapor deposition (CVD) were transferred onto (i) glass and (ii) 150 nm thick ITO on glass substrates. The transfer was completed using a sacrificial polymer (poly(methyl methacrylate); PMMA), using a method similar to that provided in previous reports.[29,50] CVD-graphene on copper was overcoated with PMMA (MW = 925k, 2% in chlorobenzene) by spin-coating at 2000 rpm. The samples were placed in copper etchant 0.2 M ammonium persulfate (APS) and then bath-ultrasonicated for 15 min to remove the bottom-facing graphene layer. The samples were left overnight (10 h) in the etchant for the copper to completely etch. After the etching, the floating PMMA on graphene was scooped out from the APS solution and refloated in DI water (×3) to rinse any residual copper etchant. The samples were then floated in 5% HF in DI water for 60 min to remove trace silica particles that might have been deposited from the CVD system during graphene growth, following which they were rinsed in DI water (×3). From the final DI water bath, the samples were scooped

onto bare glass or ITO/glass and spin-dried at 8000 rpm for 2 min to remove water trapped between the graphene sheet and the substrate. To remove the PMMA layer, the samples were placed in room-temperature acetone baths (×2) for 20 min after which they were rinsed in isopropanol for 2 min to wash away any residual acetone. Finally, they were dried using an air gun and then annealed in an Ar atmosphere for 2 h at 500 °C to remove any residual PMMA. The Ar anneal step was found to be very critical as it resulted in more atomically pristine graphene surfaces more analogous to freshly cleaved highly ordered pyrolytic graphite (HOPG). We note that ITO/graphene samples were also exposed to this Ar anneal step; therefore, the work function of ITO in ITO/graphene samples is most likely different from the unannealed ITO controls used throughout this work.

Kelvin Probe Force Microscopy. KPFM measurement was conducted using Agilent 5500 in an argon-filled controlled environment chamber under atmospheric pressure. KPFM is a technique that maps the contact potential difference (CPD) of a sample, concomitant with morphology. CPD is defined as

$$CPD_{sample} = (\varphi_{tip} - \varphi_{sample})/e \tag{4}$$

where ϕ_{tip} and ϕ_{sample} are the work functions of the conductive tip and sample, respectively, and e is the elementary charge. Generally, morphology and CPD data can either be collected simultaneously (single-pass) or separately (double-pass). The Agilent 5500 model operates as a single-pass KPFM instrument. For this work, topography, amplitude, and CPD images were captured simultaneously. The AC voltage, which generates oscillating electrical forces between the tip and sample surface, was modulated at a frequency higher than the bandwidth of morphology feedback system to prevent cross-talk between morphology and CPD measurements. Two modes of feedback response are often used in KPFM: amplitude modification (AM) mode and frequency modification (FM) mode. AM mode was chosen for this work because it yields a CPD resolution (5 meV) higher than that of FM mode (10–20 meV). The spatial resolution of AM mode is typically 25 nm.[46] All measurements were performed in an argon controlled environmental chamber to exclude measurements errors due to surface adsorbates. Before measurement, all samples were exposed to air for 3–5 min during setting up. Measurement conditions were the same for different samples. The probe tip was approached to the 90% oscillation of total oscillation to represent "contact". In the "KFM" tab, the frequency was set to 10 V, drive percentage to 10%, gain 2 as ×8, gain 3 as ×64, drive offset 2 as −3, KFM I gain as 3, P gain as 3, and set point as 0. KPFM tips (NSC18/Pt coated, 75kHZ, 2.8 N/m) were obtained from Mikromasch USA. The work function of each specific tip used for the measurement was calibrated by scanning a freshly cleaved HOPG sample with stable, known work function (4.60 eV). By using the definition $CPD_{sample} = (\phi_{tip} - \phi_{sample})/e$, the work function of the tip is calculated as $\phi_{tip} = e \cdot CPD_{HOPG} + 4.60$. Calibration was done before and after each measurement of the sample to confirm that ϕ_{tip} did not change during measurement. Morphology and CPD data were analyzed using Gwyddion.[51] To obtain the average CPD value of the interested region, the region was highlighted using the "Mark by Mask" feature and the average CPD value was obtained from the "statistical quantities" analysis.

Raman Spectroscopy. Spatially resolved Raman data were acquired with a ThermoFisher MicroRaman DXR. A 532 nm laser with 3.0 mW power and 5 s exposure time per spot was used for all the scans. The laser spot size was confined to ca. 700 nm. Raman maps were collected across a 18×18 μm^2 area with a mapping pixel size of 3×3 μm^2. The Raman spectra from all the points on the map were averaged to obtain spatially averaged spectra in each case.

■ RESULTS AND DISCUSSION

Pentacene Morphology and Intermolecular Orientation on Varied Substrates. We first deposited 100 nm pentacene thin films on oxygen plasma-cleaned bare glass and glass covered with a monolayer of graphene (graphene/glass). The crystal structure and molecular orientation of pentacene films are supported by X-ray diffraction, Raman spectra, and KPFM topography images. It has previously been reported that at least four crystal polymorphs of pentacene can be distinguished based on four different $d_{(001)}$: 14.1, 14.4, 15.1, and 15.4 Å. All four of these phases can be synthesized in thin films, while only 14.1 and 14.4 Å phases can exist in the bulk. Single-crystal pentacene adopts the 14.1 Å phase.[52−55] The transformation from 15.1 and 15.4 Å polymorphs to 14.1 and 14.4 Å polymorphs can happen at elevated temperatures.[52,53] In Figure 1, the $\theta-2\theta$ scans of 100 nm thick pentacene film grown
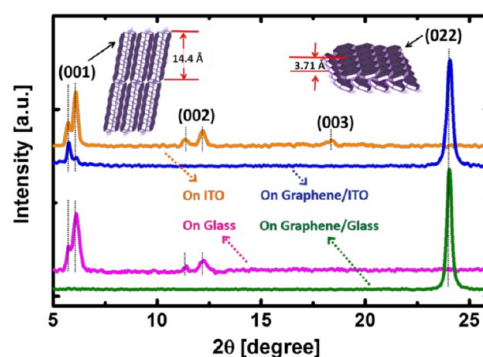

Figure 1. X-ray diffraction (XRD) $\theta-2\theta$ scans of pentacene films grown on bare glass, bare ITO, monolayer graphene-covered glass, and monolayer graphene-covered ITO.

on glass displays Bragg peaks at $2\theta = 5.71°$ and $6.15°$, with a corresponding $d_{(001)}$ of 15.4 and 14.4 Å, attributed to the thin-film phase and bulk phase of a pentacene film with standing-up molecules.[54] Bragg peaks at $2\theta = 11.40°$ and $12.19°$ represent the (002) periodicity of the thin-film and bulk phases. These Bragg peaks confirm the standing-up orientation of pentacene molecules illustrated in Figure 2a.[55,56] Pentacene films on graphene/glass show a single Bragg peak at $2\theta = 23.98°$ without a (001) peak. The corresponding d-spacing is 3.7 Å, which is characteristic of a pentacene crystal grown normal to the surface along the (022) direction (Figure 2b).[57,58]

The orientations of pentacene on glass and on graphene/glass are also confirmed by their Raman spectra. Figure 3a shows the spatially averaged Raman spectra for a 50 nm thick pentacene film on bare glass. The features at 1533, 1501, 1457, 1409, 1371, 1178, and 1158 cm^{-1} can be assigned to the A$_g$ fundamental band, and the band at 1596 cm^{-1} can be assigned to a B$_{3g}$ fundamental.[59] These Raman features originate from various vibrational modes of the C−H and C−C bonds of pentacene. It was previously established that the B$_{3g}$ bands have zero Raman intensities when the long axis of a pentacene molecule is perpendicular to the electric field vector of the laser
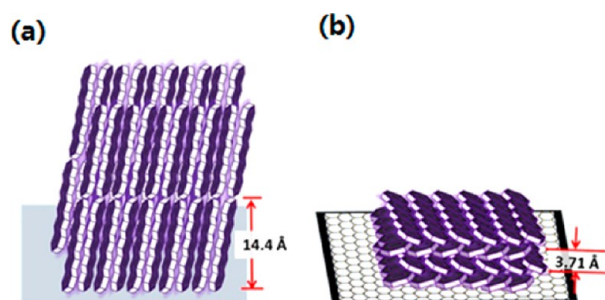
Figure 2. (a) Illustration of pentacene standing-up orientation on oxide. (b) Illustration of pentacene lying-down orientation on graphene.
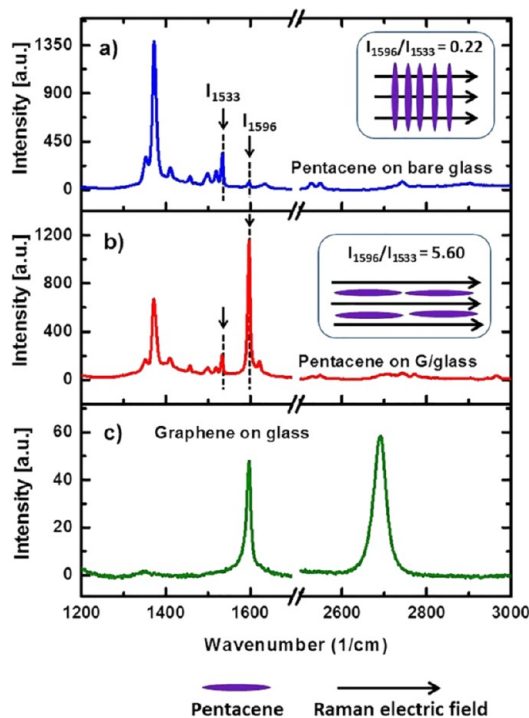
Figure 3. Spatially averaged Raman spectra of (a) pentacene on bare glass, (b) pentacene on monolayer graphene-covered glass, and (c) monolayer graphene on glass (λ = 532 nm; 3.0 mW).

used in the measurement. In particular, the ratio of the intensity of the 1596 cm^{-1} band to that of the 1533 cm^{-1} band ($R = I_{1596}/I_{1533}$) can be used to qualitatively compare the orientation of the long axis of the pentacene molecule on different substrates; an R value of zero would indicate a pentacene film with the long axis of every molecule oriented perpendicular to the substrate.[59] Using X-ray diffraction analysis, we previously established that the tilt angle of a pentacene molecule is close to 6.8° on bare glass and close to 90° on graphene, indicating that the long-axis of the pentacene molecule is almost-perpendicular and almost-parallel to the electric field vector of the laser, respectively. This observation is further verified by comparing R values obtained from the spatially averaged Raman spectra for a pentacene film on glass (Figure 3a) and on graphene (Figure 3b). For pentacene on glass, R = 0.22, whereas the same film on graphene yields R = 5.6, indicating that the orientation of the long axis is nearly perpendicular to the substrate in the former case. A significantly enhanced B$_{3g}$ band intensity and R-value indicates that the pentacene molecules are lying almost flat on the graphene surface because of an increased molecule-to-substrate interaction.

Figure 3c shows the spatially averaged Raman spectra of a monolayer of graphene on glass before any deposition of pentacene. The features at 1348, 1596, and 2691 cm^{-1} correspond to the D, G, and 2D bands of graphene.[60] The relative intensities, widths, and positions of these features provide information about the number of layers, disorder, and doping levels, among several other characteristics of the atomic membrane. In particular, the ratio of the intensity of the D-band and the G-band (I_D/I_G) is directly related to the defect density in the graphene sheet. For graphene grown via chemical vapor deposition (used in this study), an I_D/I_G < 0.1 is considered as a benchmark for a graphene sheet with very low defect density. The monolayer graphene used for this study had an I_D/I_G of 0.04, indicating that our atomic membranes have a very low defect density. Also, the relative shifts of the G and 2D bands from their intrinsic positions (1584 and 2688 cm^{-1}, respectively) reveal the nature of doping.[61] The relative shifts obtained from Figure 3c indicate that the monolayer graphene used for this study is predominantly p-doped.

Morphology and contact potential difference (CPD) images were obtained simultaneously by KPFM measurements in an argon-filled, environment-controlled chamber. The principle of KPFM and pertinent experimental details are included in Experimental Methods. The same measurement conditions were applied for all scans. Topography images (10 μm scale; Figure 4a,f) show the strikingly different shapes and densities of pentacene crystal domains on glass versus on graphene. On glass, the crystal domains are relatively isotropic and uniformly spread. On graphene, the crystal domains are anisotropic and densely cover the surface. Panels b and g of Figure 4 show the 1 μm scale topography images of pentacene thin film on glass and graphene/glass, respectively. Panels c and h of Figure 4 are the 3D images of panels b and g, respectively. Typical terracelike or pyramidal islands of pentacene crystal domains are observed on glass, which is indicative of a "standing-up" intermolecular configuration, illustrated in Figure 2a.[57] Large plank-shaped grains, or laminar islands, with relatively smooth surfaces are observed on monolayer graphene, which suggests a predominantly "lying-down" orientation of the individual molecules in the film (Figure 2b).[57]

Panels d and i in Figure 4 show the CPD images corresponding to the topography images of panedls b and g in Figure 4, respectively. The CPD signal is recorded to reveal the work function difference between the KPFM probe tip and the sample with the definition CPD$_{sample}$ = ($\phi_{tip} - \phi_{sample})/e$. Thus, the work function of the film is directly reveled by CPD. The CPD of pentacene films grown on glass and on graphene/glass (displayed in Figure 4d,i) can be correlated to their topography images. The height and CPD cross sections across two crystal domains of a pentacene film on glass (green lines in Figure 4b,d) are displayed in Figure 4e. The height profile shows that the difference between the highest domain center and lowest domain edge is about 10 nm within the two neighboring domains. The CPD profile matches the height profile with 40 mV difference across the domains. In contrast, the profile lines extracted from the pentacene on graphene/glass film show different features. The height profile displays a 6 nm difference between the domain center and edge, whereas the CPD profile shows no significant contrast (within 10 meV). Cross-talk during simultaneous morphology and CPD imaging with KPFM is minimal even in single-pass mode (see

(a)-(e) Pentacene on Glass

(f)-(j) Pentacene on Graphene/Glass
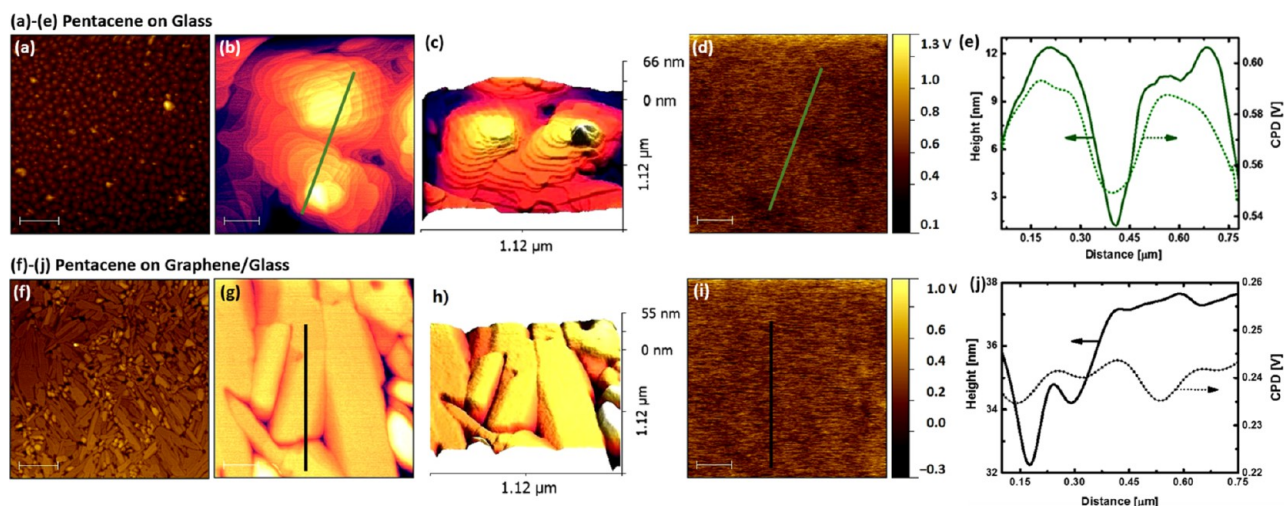
Figure 4. (a, b) Topography images of 100 nm thick pentacene film grown on glass. (c) 3D topography image corresponding to image in panel b. (d) CPD image corresponding to image in panel b measured using KPFM. (e) Profile line indicated in panels b and d. (f,g) Topography images of 100 nm thick pentacene film grown on monolayer graphene-covered glass. (h) 3D topography image corresponding to image in panel g. (i) CPD image corresponding to image in panel g measured by KPFM. (j) Profile line indicated in panels g and i. Scale bar is 2 μm in panels a and f; scale bar is 200 nm in panels b, d, g, and i.

description of KPFM measurement in Experimental Methods). The morphology and CPD images obtained for pentacene on graphene/glass reinforce this statement, as the observed local CPD image is uniform even when the corresponding morphology does not display the same uniformity. Therefore, we can conclude that the 40 meV gradual shift of CPD observed in the pentacene film on glass does not arise from cross-talk with the topography measurement. Instead, it can be attributed to the evolution of intragap states due to displacement along the long axis of neighboring pentacene molecules. Greater displacement induces gap states with more offset from the band edge. This correlation has been previously reported for the standing-up pentacene system.[62]

We also investigated the impact of monolayer graphene on the morphological and CPD properties of pentacene films on ITO-coated glass because ITO is a widely used transparent conducting electrode in optoelectronic devices. Crystal domains observed on ITO and on graphene/ITO were similar to those on glass and graphene/glass, respectively (Figure 5a,c). Notably, a few small areas of pyramidal islands, possible standing-up orientation defects, were observed for pentacene samples grown on graphene/ITO whereas no such defects were observed for pentacene samples grown on graphene/glass. One such defect area can be seen in the bottom right corner of Figure 5c. The root-mean-square (rms) roughness of the pyramidal crystal domain on ITO was 10.74 nm; the rms roughness of the laminar region was 7.15 nm; and that of the pyramidal defect was 10.27 nm, which is similar to the rms roughness of the pyramidal domains on ITO (see Figure S1 in the Supporting Information for a profile of the relative roughness of various pentacene domains). These roughness details suggest that the pyramidal defects in the pentacene films grown on graphene/ITO arise because of the standing-up configuration observed on either bare ITO or bare glass. XRD data (see Figure 1) confirm the standing-up orientation on ITO with (001), (002), and (003) characteristic peaks and corroborate the presence of standing-up pentacene on graphene/ITO, with small peaks at $2\theta = 5.71°$ and $6.15°$ along with the dominant Bragg peak at $2\theta = 23.98°$

(a)-(b) Pentacene on ITO
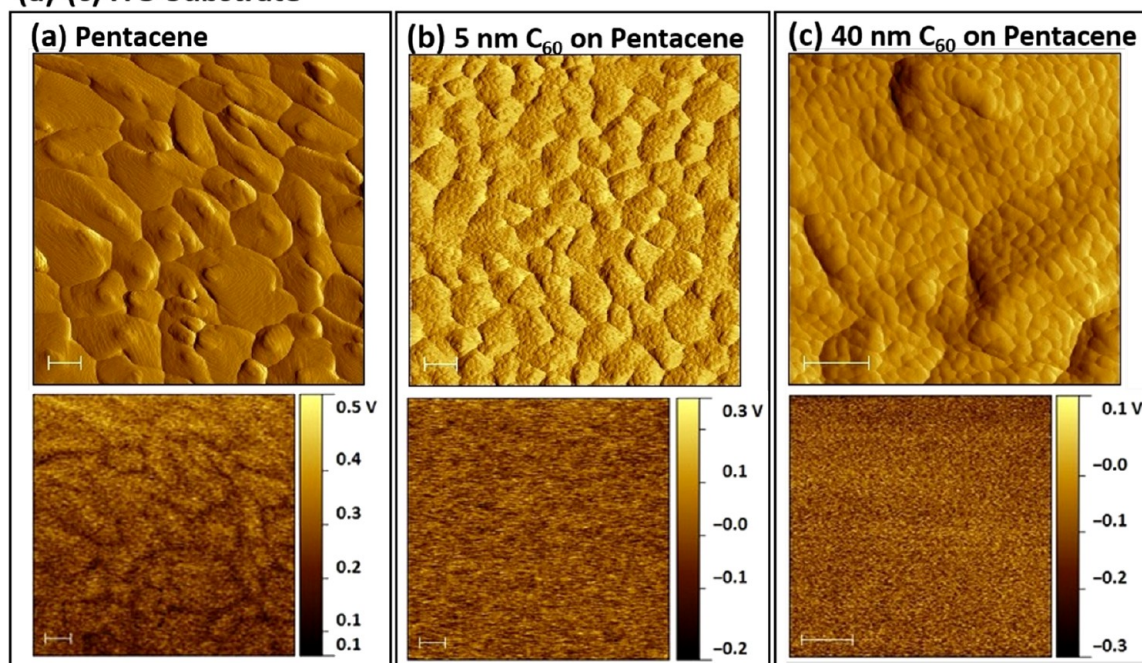
(c)-(d) Pentacene on Graphene/ITO
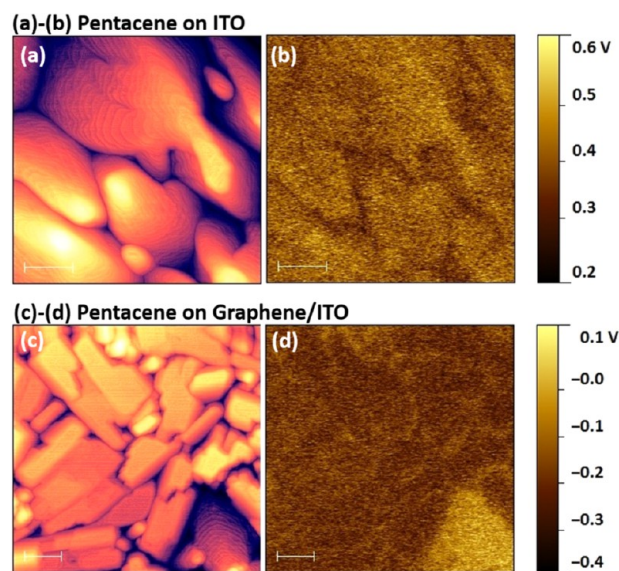
Figure 5. (a) Topography image of a 100 nm thick pentacene film grown on bare ITO and (b) the corresponding CPD image measured using KPFM. (c) Topography image of a 100 nm thick pentacene film grown on monolayer graphene-covered ITO and (d) the corresponding CPD image. Scale bar is 200 nm in all images.

representing the lying-down orientation. We posit that these pyramidal defects arise because of holes or tears in the graphene samples that are either inherited from the growth process or are introduced during the transfer process.

XRD spectra, Raman spectra, and topography images confirmed that pentacene adopts a standing-up orientation on glass and on ITO, all lying-down orientation on graphene/glass, and a majority of pentacene grains adopt a lying-down orientation on graphene/ITO, accompanied by a few defect regions of standing-up orientation due to holes or tears in graphene, as discussed above.

Energy Levels of Heterojunctions Involving Pentacene with Different Orientations. The surface electrostatic potential of a thin film defines the vacuum level in the

(a)-(c) ITO Substrate

(d)-(f) Graphene/ITO Substrate
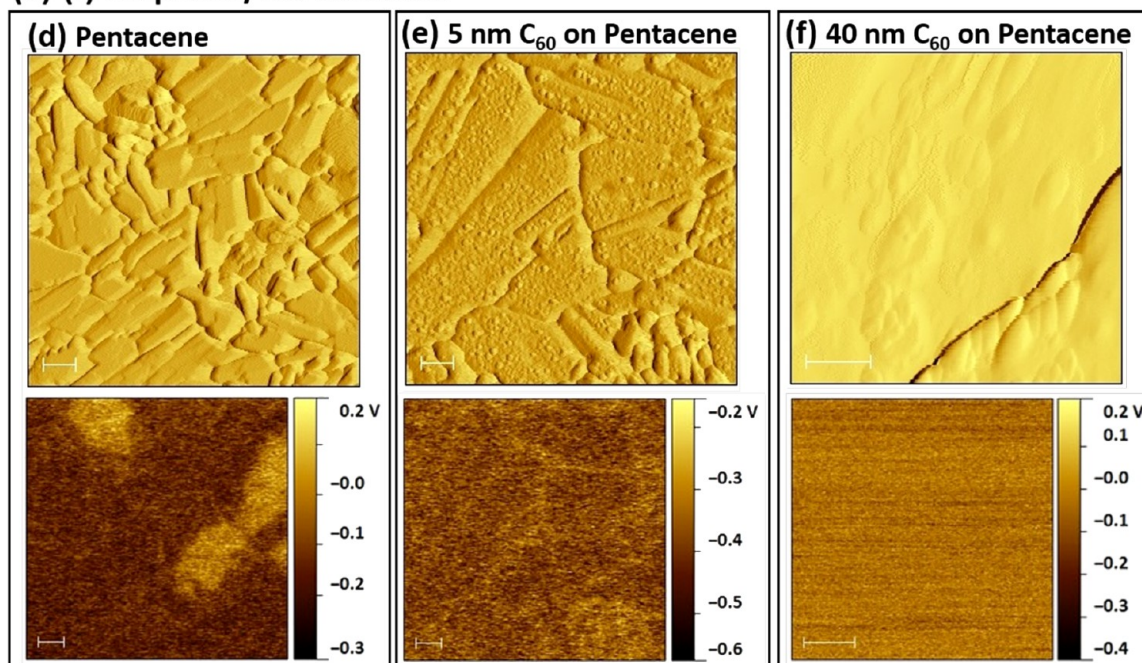
Figure 6. (a,d) Amplitude and corresponding CPD images measured by KPFM of 100 nm pentacene, (b,e) 5 nm C_{60} grown on pentacene, and (c,f) 40 nm C_{60} grown on pentacene; (a–c) on glass substrate, and (d–f) on graphene/glass substrate. In each box, the top image is amplitude, the bottom image is the corresponding CPD. Scale bar is 200 nm in all images.

electronic band structure of the materials comprising the film. For an ordered, structurally anisotropic organic semiconductor thin film, the surface electrostatic potential and IP and EA levels are highly molecular orientation-dependent. As a result, the Fermi level, IP, or EA levels of the organic semiconductor and the substrate Fermi level can be tuned by molecular orientation. Panels b and d in Figure 5 are CPD images corresponding to panels a and c in Figure 5, respectively. To calculate the work function of films from CPD, the work function of the Pt-coated tip used in this study was separately calibrated by scanning a

standard sample, highly ordered pyrolytic graphite, with a known work function (ϕ_{HOPG} = 4.60 eV[45]). By using the definition $CPD_{HOPG} = (\phi_{tip} - \phi_{HOPG})/e$, the work function of tip can be obtained as $\phi_{tip} = e \cdot CPD_{HOPG} + 4.60$. Calibrations were performed before and after each reported CPD measurement to confirm that charge accumulation did not erroneously change the work function of the tip. Surface potential data were analyzed using Gwyddion,[51] and statistically averaged CPD values of films were obtained using the "statistical" analysis tab. Using the "mark by mask" feature of Gwyddion, the local CPD

(work function) of the two distinct regions in Figure 5d can be obtained separately. The data workup procedure is detailed in Figure S2 in the Supporting Information.

Using the calibrated work function of the Pt tip, the work function of 100 nm pentacene is calculated to be 4.53 eV on ITO (calculated from CPD of the entire image of Figure 5b). The local work function of lying-down pentacene is 4.89 eV on graphene/ITO, and that of standing-up pentacene on ITO is 4.68 eV (calculated from CPD of darker and lighter regions of Figure 5d, respectively). Pentacene−ITO and pentacene−graphene interfaces are both in the category of noninteracting heterojunctions. Thus, the interfacial energy level alignment associated with the interfacial charge transfer can be explained by the gap-states model.[22] It has been acknowledged that the density of gap states can determine interfacial energy level alignment in many systems.[39] Before contact, the work function of oxygen plasma-treated ITO (4.76 eV as measured by KPFM) is larger than the energy level of occupied gap states of the standing-up pentacene film. Upon contact, spontaneous charge transfer from pentacene to ITO induces Fermi level pinning to the pentacene gap states until equilibrium is reached. This phenomenon results in an observed Fermi level of 4.53 eV for standing-up pentacene on oxygen plasma-treated ITO (Figure 5b). The work function of lying-down pentacene on graphene/ITO is 4.89 eV and that of graphene/ITO is 4.90 eV. Hence, we conclude that vacuum level alignment is observed for lying-down pentacene on graphene/ITO. We infer that the work function of graphene (4.90 eV) is located deep in the band gap of lying-down pentacene. This difference is attributed to the higher-lying IP of lying-down pentacene (5.25 eV) compared to that of standing-up pentacene (4.90 eV),[63] which is caused by the exposed π electrons of lying-down pentacene. The gap states, which exponentially decay from the band edge, accordingly vary in energy levels. The varying energy levels of these pentacene gap states, in concert with the substrate work function, determine whether a vacuum level alignment or Fermi level pinning mechanism dominates.

It is interesting to note from 1 μm scale images (Figure 5d) that KPFM spatially resolves local work function differences arising from both local vacuum level alignment or Fermi level pinning mechanisms. The substrate work function of bare ITO is 4.76 eV, and that of graphene/ITO is 4.90 eV. Thus, the substrate Fermi level can be pinned to different pentacene gap states, most likely due to a greater amount of charge transfer between pentacene and a higher work function substrate. Hence, the Fermi level of standing pentacene is 4.53 eV on bare ITO but is 4.68 eV on graphene/ITO.

The work function of organic−organic heterojunctions were further investigated by examining pentacene−C$_{60}$ heterojunctions grown either on ITO or graphene/ITO. The amplitude and CPD images obtained using KPFM are provided in Figure 6. The amplitude image is a map showing the deviation of the AFM tip oscillation from the set-point, which can reveal fine morphological features better than topography images. The amplitude images of standing-up pentacene on ITO (Figure 6a) and lying-down pentacene on graphene (Figure 6d) show similar features as those seen in the topography images in Figure 5. A 5 nm C$_{60}$ film deposited on standing-up pentacene (Figure 6b) displayed uniform surface coverage. With this highly conformal covering of structurally symmetric C$_{60}$, the CPD contrast shown in Figure 6a largely vanishes. On the contrary, small C$_{60}$ aggregates are observed for 5 nm thick C$_{60}$ films grown on graphene-templated lying-down pentacene

(Figure 6e), and the corresponding CPD image also displays less uniformity than the C$_{60}$ films grown on untemplated standing-up pentacene. We ascribe this difference to the terminating layer of the pentacene film. The terminating layer of standing-up pentacene films comprises primarily aryl hydrogen atoms, which interact with C$_{60}$ equivalently. The surface of the lying-down pentacene film is more complicated, comprising both the π-electron cloud of the pentacene molecule and aryl hydrogen atoms. In this case, it is possible that C$_{60}$ preferentially nucleates at specific positions over others. Furthermore, if thicker (40 nm) films of C$_{60}$ are deposited onto pentacene, all structural anisotropies are fully blurred (Figure 6c,f) and no CPD contrast can be observed. In this case, the CPD images reveal the uniform local work function of C$_{60}$ film on pentacene.

The work function calculated from the CPD scan of a 40 nm thick film of C$_{60}$ on standing-up pentacene was 4.99 eV, and that of a 40 nm thick film of C$_{60}$ on lying-down pentacene was 5.01 eV. Obvious vacuum level shifts at the pentacene−C$_{60}$ interface were observed in our films, contrary to prior reports of vacuum level alignment for the same pentacene−C$_{60}$ heterojunctions.[64] This difference is ascribed to the presence of gap states in our sample: the unoccupied gap states of C$_{60}$ tail to 5 eV in our samples; thus, they are energetically accessible to both the Fermi levels of standing-up pentacene on ITO (4.53 eV) and lying-down pentacene on graphene/ITO (4.89 eV). After deposition of C$_{60}$, the Fermi levels of both pentacene and C$_{60}$ are pinned to the C$_{60}$ gap states that lie between 4.99 and 5.01 eV. The anomalous deep-lying gap states in our C$_{60}$ films most likely arose because of a vacuum break (with nitrogen vent) between the deposition of pentacene and C$_{60}$ and subsequent air and light exposure during sample transfer to our KPFM instrument. In comparison, previous reports detailing vacuum level alignment in pentacene−C$_{60}$ heterojunctions used samples that were prepared and measured in ultrahigh vacuum ($\sim 10^{-9}-10^{-10}$ Torr) without an intervening vacuum break.[64] We also attribute the high work function of our C$_{60}$ films to interfacial molecular rearrangement.[65]

Previously measured work function values for pentacene and C$_{60}$[66] were used, along with previously reported ionization potential values, to construct the energy band diagrams depicted in Figure 7. From Figure 7, we see that the pentacene−C$_{60}$ heterojunction shows a built-in voltage on bare ITO larger than that on graphene-covered ITO. This observation reveals that, even within the same material, molecular orientations in ordered crystalline thin films can have significant impact on ultimate device performance.

■ CONCLUSIONS

The morphology and electronic properties of pentacene on oxides and graphene were investigated by spatially resolved KPFM measurements. Different work functions of pentacene on bare ITO (4.53 eV) and on graphene/ITO (4.89 eV) were observed and were attributed to Fermi level pinning and vacuum level alignment, respectively. The magnitude of the observed work function difference is significant, which will, in turn, have significant ramifications on the built-in voltage of pentacene−C$_{60}$ heterojunctions. Furthermore, coexisting standing-up and lying-down pentacene were observed in 1 μm scale KPFM images of pentacene films grown on graphene/ITO substrates containing holes in the template graphene layer. A corresponding local work function difference was recorded for
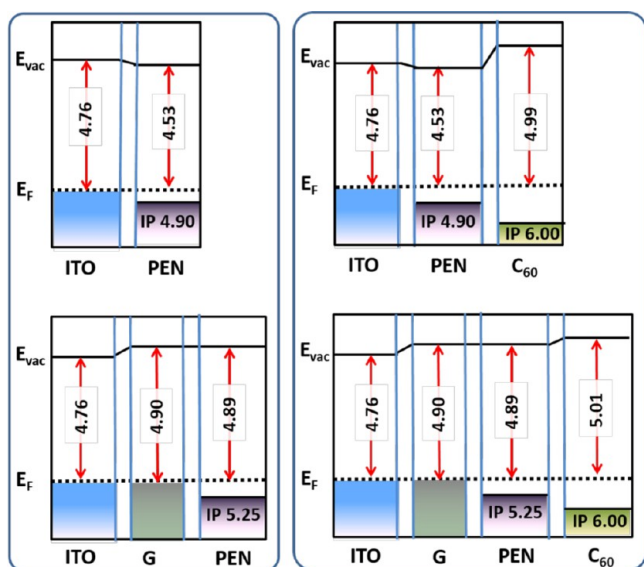
Figure 7. Illustration of the energy level alignment across the pentacene–ITO, pentacene–graphene/ITO interface, and C_{60}–pentacene interface on either substrate. Work functions were measured in this study using KPFM after each layer was transferred or deposited. Valence band edges are extracted from prior UPS measurements. Overall, Fermi level pinning occurs across the standing penacene–ITO interface, while vacuum level alignment holds across the lying pentacene–graphene/ITO interface. After deposition of C_{60}, both Fermi levels are pinned to the C_{60} gap states.

these two regions as 4.68 and 4.89 eV, respectively, indicating that KPFM is a powerful method with which to visualize the transition from local Fermi level pinning to vacuum level alignment in organic semiconductor thin films. The data detailed herein provide a fundamental picture of the various morphological and electronic interfacial effects active in optoelectronic devices containing a bare graphene electrode.

ASSOCIATED CONTENT

ⓢ Supporting Information
Height cross sections of AFM scans and detailed description of CPD data analysis. This material is available free of charge via the Internet at http://pubs.acs.org.

AUTHOR INFORMATION

Corresponding Author
*Department of Chemistry, University of Wisconsin-Madison, 1101 University Ave, Madison, WI 53706. Tel.: 608-262-1502. E-mail: tandrew@chem.wisc.edu.

Notes
The authors declare no competing financial interest.

ACKNOWLEDGMENTS

REFERENCES

(1) Barr, M. C.; Rowehl, J. A.; Lunt, R. R.; Xu, J.; Wang, A.; Boyce, C. M.; Im, S. G.; Bulovic, V.; Gleason, K. K. Direct Monolithic Integration of Organic Photovoltaic Circuits on Unmodified Paper. *Adv. Mater. (Weinheim, Ger.)* **2011**, 23, 3499−3505.

(2) Krebs, F. C.; Gevorgyan, S. A.; Alstrup, J. A Roll-to-Roll Process to Flexible Polymer Solar Cells: Model Studies, Manufacture and Operational Stability Studies. *J. Mater. Chem.* **2009**, 19, 5442−5451.

(3) Krebs, F. C.; Norrman, K. Using Light-Induced Thermocleavage in a Roll-to-Roll Process for Polymer Solar Cells. *ACS Appl. Mater. Interfaces* **2010**, 2, 877−887.

(4) Scharber, M. C.; Sariciftci, N. S. Efficiency of Bulk-Heterojunction Organic Solar Cells. *Prog. Polym. Sci.* **2013**, 38, 1929−1940.

(5) Shirota, Y.; Kageyama, H. Charge Carrier Transporting Molecular Materials and Their Applications in Devices. *Chem. Rev. (Washington, DC, U.S.)* **2007**, 107, 953−1009.

(6) Polman, A.; Atwater, H. A. Plasmonics for Improved Photovoltaic Devices. *Nat. Mater.* **2010**, 9, 205−214.

(7) Ferry, V. E.; Munday, J. N.; Atwater, H. A. Design Considerations for Plasmonic Photovoltaics. *Adv. Mater. (Weinheim, Ger.)* **2010**, 22, 4794−4808.

(8) Ameri, T.; Li, N.; Brabec, C. J. Highly Efficient Organic Tandem Solar Cells: A Follow Up Review. *Energy Environ. Sci.* **2013**, 6, 2390−2413.

(9) Siddiki, M. K.; Li, J.; Galipeau, D.; Qiao, Q. A review of Polymer Multijunction Solar Cells. *Energy Environ. Sci.* **2010**, 3, 867−883.

(10) Amy, F.; Chan, C.; Kahn, A. Polarization at the Gold/Pentacene Interface. *Org. Electron.* **2005**, 6, 85−91.

(11) Hill, I. G.; Milliron, D.; Schwartz, J.; Kahn, A. Organic Semiconductor Interfaces: Electronic Structure and Transport Properties. *Appl. Surf. Sci.* **2000**, 166, 354−362.

(12) Cahen, D.; Kahn, A. Electron Energetics at Surfaces and Interfaces: Concepts and Experiments. *Adv. Mater. (Weinheim, Ger.)* **2003**, 15, 271−277.

(13) Peumans, P.; Yakimov, A.; Forrest, S. R. Small Molecular Weight Organic Thin-Film Photodetectors and Solar Cells. *J. Appl. Phys.* **2003**, 93, 3693−3723.

(14) Lee, W. H.; Park, J.; Sim, S. H.; Lim, S.; Kim, K. S.; Hong, B. H.; Cho, K. Surface-Directed Molecular Assembly of Pentacene on Monolayer Graphene for High-Performance Organic Transistors. *J. Am. Chem. Soc.* **2011**, 133, 4447−4454.

(15) Bernardo, B.; Cheyns, D.; Verreet, B.; Schaller, R. D.; Rand, B. P.; Giebink, N. C. Delocalization and Dielectric Screening of Charge Transfer States in Organic Photovoltaic Cells. *Nat. Commun.* **2014**, 5, 3245−3251.

(16) Jailaubekov, A. E.; Willard, A. P.; Tritsch, J. R.; Chan, W.-L.; Sai, N.; Gearba, R.; Kaake, L. G.; Williams, K. J.; Leung, K.; Rossky, P. J.; et al. Hot Charge-Transfer Excitons Set the Time Limit for Charge Separation at Donor/Acceptor Interfaces in Organic Photovoltaics. *Nat. Mater.* **2013**, 12, 66−73.

(17) Verlaak, S.; Beljonne, D.; Cheyns, D.; Rolin, C.; Linares, M.; Castet, F.; Cornil, J.; Heremans, P. Electronic Structure and Geminate Pair Energetics at Organic−Organic Interfaces: The Case of Pentacene/C_{60} Heterojunctions. *Adv. Funct. Mater.* **2009**, 19, 3809−3814.

(18) Yi, Y.; Coropceanu, V.; Brédas, J.-L. Exciton-Dissociation and Charge-Recombination Processes in Pentacene/C_{60} Solar Cells: Theoretical Insight into the Impact of Interface Geometry. *J. Am. Chem. Soc.* **2009**, 131, 15777−15783.

(19) Chen, W.; Qi, D.-C.; Huang, H.; Gao, X.; Wee, A. T. S. Organic−Organic Heterojunction Interfaces: Effect of Molecular Orientation. *Adv. Funct. Mater.* **2011**, 21, 410−424.

(20) Duhm, S.; Heimel, G.; Salzmann, I.; Glowatzki, H.; Johnson, R. L.; Vollmer, A.; Rabe, J. P.; Koch, N. Orientation-Dependent Ionization Energies and Interface Dipoles in Ordered Molecular Assemblies. *Nat. Mater.* **2008**, 7, 326−332.

52

dx.doi.org/10.1021/jp508931e | *J. Phys. Chem. C* 2015, 119, 45−54

(21) Heimel, G.; Salzmann, I.; Duhm, S.; Koch, N. Design of Organic Semiconductors from Molecular Electrostatics. *Chem. Mater.* **2011**, *23*, 359−377.

(22) Zhong, J. Q.; Mao, H. Y.; Wang, R.; Qi, D. C.; Cao, L.; Wang, Y. Z.; Chen, W. Effect of Gap States on the Orientation-Dependent Energy Level Alignment at the DIP/$F_{16}CuPc$ Donor−Acceptor Heterojunction Interfaces. *J. Phys. Chem. C* **2011**, *115*, 23922−23928.

(23) Yost, S. R.; Van Voorhis, T. Electrostatic Effects at Organic Semiconductor Interfaces: A Mechanism for "Cold" Exciton Breakup. *J. Phys. Chem. C* **2013**, *117*, 5617−5625.

(24) Yost, S. R.; Wang, L.-P.; Van Voorhis, T. Molecular Insight into the Energy Levels at the Organic Donor/Acceptor Interface: A Quantum Mechanics/Molecular Mechanics Study. *J. Phys. Chem. C* **2011**, *115*, 14431−14436.

(25) Duhm, S.; Salzmann, I.; Heimel, G.; Oehzelt, M.; Haase, A.; Johnson, R. L.; Rabe, J. P.; Koch, N. Controlling Energy Level Offsets in Organic/Organic Heterostructures Using Intramolecular Polar Bonds. *Appl. Phys. Lett.* **2009**, *94*, 033304.

(26) Baldacchini, C.; Allegretti, F.; Gunnella, R.; Betti, M. G. Molecule−Metal Interaction of Pentacene on Copper Vicinal Surfaces. *Surf. Sci.* **2007**, *601*, 2603−2606.

(27) Bagus, P. S.; Hermann, K.; Woll, C. The Interaction of C_6H_6 and C_6H_{12} with Noble Metal Surfaces: Electronic Level Alignment and the Origin of the Interface Dipole. *J. Chem. Phys.* **2005**, *123*, 184109.

(28) Ishii, H.; Sugiyama, K.; Ito, E.; Seki, K. Energy Level Alignment and Interfacial Electronic Structures at Organic/Metal and Organic/Organic Interfaces. *Adv. Mater. (Weinheim, Ger.)* **1999**, *11*, 605−625.

(29) Singha Roy, S.; Bindl, D. J.; Arnold, M. S. Templating Highly Crystalline Organic Semiconductors Using Atomic Membranes of Graphene at the Anode/Organic Interface. *J. Phys. Chem. Lett.* **2012**, *3*, 873−878.

(30) Witte, G.; Wöll, C. Growth of Aromatic Molecules on Solid Substrates for Applications in Organic Electronics. *J. Mater. Res.* **2011**, *19*, 1889−1916.

(31) Crispin, A.; Crispin, X.; Fahlman, M.; Berggren, M.; Salaneck, W. R. Transition between Energy Level Alignment Regimes at Low Band Gap Polymer-Electrode Interfaces. *Appl. Phys. Lett.* **2006**, *89*, 213503.

(32) Koch, N.; Vollmer, A. Electrode-Molecular Semiconductor Contacts: Work-Function-Dependent Hole Injection Barriers versus Fermi-Level Pinning. *Appl. Phys. Lett.* **2006**, *89*, 162107.

(33) Tengstedt, C.; Osikowicz, W.; Salaneck, W. R.; Parker, I. D.; Hsu, C.-H.; Fahlman, M. Fermi-Level Pinning at Conjugated Polymer Interfaces. *Appl. Phys. Lett.* **2006**, *88*, 053502.

(34) Vandewal, K.; Albrecht, S.; Hoke, E. T.; Graham, K. R.; Widmer, J.; Douglas, J. D.; Schubert, M.; Mateker, W. R.; Bloking, J. T.; George, F. B.; et al. Efficient Charge Generation by Relaxed Charge-Transfer States at Organic Interfaces. *Nat. Mater.* **2014**, *13*, 63−68.

(35) Zhu, X. Y.; Yang, Q.; Muntwiler, M. Charge-Transfer Excitons at Organic Semiconductor Surfaces and Interfaces. *Acc. Chem. Res.* **2009**, *42*, 1779−1787.

(36) Romaner, L.; Heimel, G.; Brédas, J.-L.; Gerlach, A.; Schreiber, F.; Johnson, R.; Zegenhagen, J.; Duhm, S.; Koch, N.; Zojer, E. Impact of Bidirectional Charge Transfer and Molecular Distortions on the Electronic Structure of a Metal-Organic Interface. *Phys. Rev. Lett.* **2007**, *99*, 256801.

(37) Toyoda, K.; Hamada, I.; Lee, K.; Yanagisawa, S.; Morikawa, Y. Density Functional Theoretical Study of Pentacene/Noble Metal Interfaces with van der Waals Corrections: Vacuum Level Shifts and Electronic Structures. *J. Chem. Phys.* **2010**, *132*, 134703.

(38) Braun, S.; Salaneck, W. R.; Fahlman, M. Energy-Level Alignment at Organic/Metal and Organic/Organic Interfaces. *Adv. Mater. (Weinheim, Ger.)* **2009**, *21*, 1450−1472.

(39) Zhong, S.; Zhong, J. Q.; Mao, H. Y.; Zhang, J. L.; Lin, J. D.; Chen, W. The Role of Gap States in the Energy Level Alignment at the Organic-Organic Heterojunction Interfaces. *Phys. Chem. Chem. Phys.* **2012**, *14*, 14127−14141.

(40) Hwang, J.; Kim, E. G.; Liu, J.; Brédas, J.-L.; Duggal, A.; Kahn, A. Photoelectron Spectroscopic Study of the Electronic Band Structure of Polyfluorene and Fluorene-Arylamine Copolymers at Interfaces. *J. Phys. Chem. C* **2007**, *111*, 1378−1384.

(41) Winkler, S.; Frisch, J.; Amsalem, P.; Krause, S.; Timpel, M.; Stolte, M.; Würthner, F.; Koch, N. Impact of Molecular Dipole Moments on Fermi Level Pinning in Thin Films. *J. Phys. Chem. C* **2014**, *118*, 11731−11737.

(42) Peisert, H.; Knupfer, M.; Schwieger, T.; Auerhammer, J. M.; Golden, M. S.; Fink, J. Full Characterization of the Interface between the Organic Semiconductor Copper Phthalocyanine and Gold. *J. Appl. Phys.* **2002**, *91*, 4872.

(43) Niederhausen, J.; Amsalem, P.; Wilke, A.; Schlesinger, R.; Winkler, S.; Vollmer, A.; Rabe, J. P.; Koch, N. Doping of C_{60} (sub)monolayers by Fermi-Level Pinning Induced Electron Transfer. *Phys. Rev. B: Condens. Matter Mater. Phys.* **2012**, *86*, 081411(R).

(44) Palermo, V.; Palma, M.; Samorì, P. Electronic Characterization of Organic Thin Films by Kelvin Probe Force Microscopy. *Adv. Mater. (Weinheim, Ger.)* **2006**, *18*, 145−164.

(45) Melitz, W.; Shen, J.; Lee, S.; Lee, J. S.; Kummel, A. C.; Droopad, R.; Yu, E. T. Scanning Tunneling Spectroscopy and Kelvin Probe Force Microscopy Investigation of Fermi Energy Level Pinning Mechanism on InAs and InGaAs Clean Surfaces. *J. Appl. Phys.* **2010**, *108*, 023711.

(46) Melitz, W.; Shen, J.; Kummel, A. C.; Lee, S. Kelvin Probe Force Microscopy and Its Application. *Surf. Sci. Rep.* **2011**, *66*, 1−27.

(47) Tal, O.; Gao, W.; Chan, C. K.; Kahn, A.; Rosenwaks, Y. Measurement of Interface Potential Change and Space Charge Region Across Metal/Organic/Metal Structures Using Kelvin Probe Force Microscopy. *Appl. Phys. Lett.* **2004**, *85*, 4148.

(48) Ogawa, Y.; Niu, T.; Wong, S. L.; Tsuji, M.; Wee, A. T. S.; Chen, W.; Ago, H. Self-Assembly of Polar Phthalocyanine Molecules on Graphene Grown by Chemical Vapor Deposition. *J. Phys. Chem. C* **2013**, *117*, 21849−21855.

(49) Mao, H. Y.; Wang, R.; Wang, Y.; Niu, T. C.; Zhong, J. Q.; Huang, M. Y.; Qi, D. C.; Loh, K. P.; Wee, A. T. S.; Chen, W. Chemical Vapor Deposition Graphene as Structural Template to Control Interfacial Molecular Orientation of Chloroaluminium Phthalocyanine. *Appl. Phys. Lett.* **2011**, *99*, 093301.

(50) Li, X.; Zhu, Y.; Cai, W.; Borysiak, M.; Han, B.; Chen, D.; Piner, R. D.; Colombo, L.; Ruoff, R. S. Transfer of Large-Area Graphene Films for High-Performance Transparent Conductive Electrodes. *Nano Lett.* **2009**, *9*, 4359−4363.

(51) Nečas, D.; Klapetek, P. Gwyddion: An Open-Source Software for SPM Data Analysis. *Cent. Eur. J. Phys.* **2012**, *10*, 181−188.

(52) Mattheus, C. C.; Dros, A. B.; Baas, J.; Oostergetel, G. T.; Meetsma, A.; de Boer, J. L.; Palstra, T. T. M. Identification of Polymorphs of Pentacene. *Synth. Met.* **2003**, *138*, 475−481.

(53) Bouchoms, I. P. M.; Schoonveld, W. A.; Vrijmoeth, J.; Klapwijk, T. M. Morphology Identification of the Thin Film Phases of Vacuum Evaporated Pentacene on SiO_2 Substrates. *Synth. Met.* **1999**, *104*, 175−178.

(54) Srnanek, R.; Jakabovic, J.; Dobrocka, E.; Irmer, G.; Heinemeyer, U.; Broch, K.; Schreiber, F.; Vincze, A.; Machovic, V.; Kovac, J.; et al. Evidence of Pentacene Bulk and Thin Film Phase Transformation into an Orthorhombic Phase by Iodine Diffusion. *Chem. Phys. Lett.* **2010**, *484*, 299−303.

(55) Yoshida, H.; Inaba, K.; Sato, N. X-ray Diffraction Reciprocal Space Mapping Study of the Thin Film Phase of Pentacene. *Appl. Phys. Lett.* **2007**, *90*, 181930.

(56) Cheng, H.-L.; Mai, Y.-S.; Chou, W.-Y.; Chang, L.-R.; Liang, X.-W. Thickness-Dependent Structural Evolutions and Growth Models in Relation to Carrier Transport Properties in Polycrystalline Pentacene Thin Films. *Adv. Funct. Mater.* **2007**, *17*, 3639−3649.

(57) Berke, K.; Tongay, S.; McCarthy, M. A.; Rinzler, A. G.; Appleton, B. R.; Hebard, A. F. Current Transport across the Pentacene/CVD-Grown Graphene Interface for Diode Applications. *J. Phys.: Condens. Matter* **2012**, *24*, 255802.

(58) Götzen, J.; Käfer, D.; Wöll, C.; Witte, G. Growth and Structure of Pentacene Films on Graphite: Weak Adhesion as a Key for Epitaxial

Film Growth. *Phys. Rev. B: Condens. Matter Mater. Phys.* **2010**, *81*, 085440.

(59) Seto, K.; Furukawa, Y. Study on Solid Structure of Pentacene Thin Films Using Raman Imaging. *J. Raman Spectrosc.* **2012**, *43*, 2015−2019.

(60) Ferrari, A. C. Raman Spectroscopy of Graphene and Graphite: Disorder, Electron−Phonon Coupling, Doping and Nonadiabatic Effects. *Solid State Commun.* **2007**, *143*, 47−57.

(61) Das, A.; Pisana, S.; Chakraborty, B.; Piscanec, S.; Saha, S. K.; Waghmare, U. V.; Novoselov, K. S.; Krishnamurthy, H. R.; Geim, A. K.; Ferrari, A. C.; et al. Monitoring Dopants by Raman Scattering in an Electrochemically Top-Gated Graphene Transistor. *Nat. Nanotechnol.* **2008**, *3*, 210−215.

(62) Kang, J. H.; da Silva Filho, D.; Bredas, J.-L.; Zhu, X. Y. Shallow Trap States in Pentacene Thin Films from Molecular Sliding. *Appl. Phys. Lett.* **2005**, *86*, 152115.

(63) Liu, X.; Grüneis, A.; Haberer, D.; Fedorov, A. V.; Vilkov, O.; Strupinski, W.; Pichler, T. Tunable Interface Properties between Pentacene and Graphene on the SiC Substrate. *J. Phys. Chem. C* **2013**, *117*, 3969−3975.

(64) Salzmann, I.; Duhm, S.; Opitz, R.; Johnson, R. L.; Rabe, J. P.; Koch, N. Structural and Electronic Properties of Pentacene-Fullerene Heterojunctions. *J. Appl. Phys.* **2008**, *104*, 114518.

(65) Mao, H. Y.; Wang, R.; Huang, H.; Wang, Y. Z.; Gao, X. Y.; Bao, S. N.; Wee, A. T. S.; Chen, W. Tuning of C_{60} Energy Levels Using Orientation-Controlled Phthalocyanine Films. *J. Appl. Phys.* **2010**, *108*, 053706.

(66) Kang, S. J.; Yi, Y.; Kim, C. Y.; Cho, S. W.; Noh, M.; Jeong, K.; Whang, C. N. Energy Level Diagrams of C_{60}/Pentacene/Au and Pentacene/C_{60}/Au. *Synth. Met.* **2006**, *156*, 32−37.

54

dx.doi.org/10.1021/jp508931e | *J. Phys. Chem. C* 2015, 119, 45−54